Hollow Co@HCN Derived from ZIF-67 as a Highly Efficient Catalyst for Hydrogenation of *o*-Cresol to *o*-Methyl Cyclohexanol

Chaoqun Fan[1] · Hang Zhu[1] · Jiuxuan Zhang[1] · Hong Jiang[1] · Rizhi Chen[1]

Abstract

The selective hydrogenation of *o*-cresol to produce *o*-methyl cyclohexanol, an important chemical intermediate, is an attractive approach. The design and development of efficient non-precious metal catalysts for the selective *o*-cresol hydrogenation remain a great challenge. Herein, cobalt nanoparticles embedded in nitrogen-doped carbon with hollow structure (Co@HCN) were fabricated by direct pyrolysis of hollow zeolitic imidazolate framework-67 (HZIF-67), and were applied in the selective hydrogenation of *o*-cresol to *o*-methyl cyclohexanol for the first time. The pyrolysis temperature and $Co(NO_3)_2·6H_2O$ concentration jointly regulate the morphology and physicochemical properties of the Co@HCN-T-x catalysts (T represents the pyrolysis temperature and x represents the $Co(NO_3)_2·6H_2O$ concentration in octanol), and significantly affect their catalytic properties. Co@HCN-500-0.1 exhibits superior catalytic activity, which is 3.3 times higher than Co@HCN-700-0.1 and 1.3 times higher than Co@HCN-500-0.4. Large ratio of meso-/macro-porous specific surface area and pore volume, small Co size with uniform dispersion, and abundant surface Co and CoN_x contents together contribute to the superior catalytic activity of Co@HCN-500-0.1. More importantly, Co@HCN-500-0.1 displays convenient magnetic recoverability, superior catalytic recyclability and universal applicability. This work provides significant insights for the design of efficient non-precious metal catalysts to be applied in the selective hydrogenation of *o*-cresol.

Graphical Abstract

Hollow Co@HCN nanospheres were synthesized by one-step pyrolysis of HZIF-67, and the morphology, pore structure, Co size and distribution, surface composition, and yield can be adjusted by the pyrolysis temperature and $Co(NO_3)2·6H_2O$ concentration. The presence of the hollow shell layer not only enhances the diffusion of the reactants, but also facilitates the dispersion and exposure of Co species, which in turn improves the catalytic performance for the selective hydrogenation of *o*-cresol to *o*-methyl cyclohexanol.
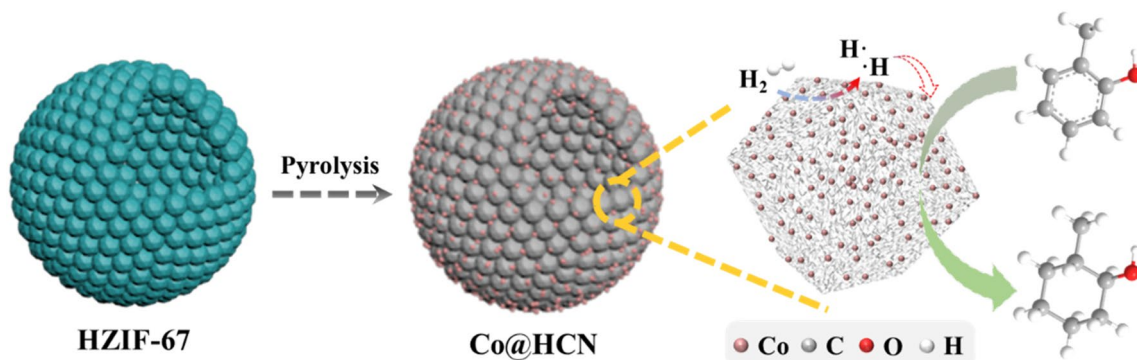
✉ Hong Jiang
hjiang@njtech.edu.cn

Extended author information available on the last page of the article

🍃 Springer

1 Introduction

o-Methyl cyclohexanol is an important intermediate for the synthesis of *o*-methyl cyclohexyl acetate, and is also used as a solvent for rubber and resin, and a colorant for drugs and food, etc. [1]. At present, the hydrogenation of *o*-cresol [2], the borohydride oxidation of methyl cyclohexene [3], the chemical enzyme synthesis [4] and many other methods [5] have been successfully applied to synthesize *o*-methyl cyclohexanol. *o*-Cresol, as one of the simpler phenolic model compounds in lignin, is widely available and vastly abundant [6]. More importantly, as compared to other synthesis methods, the *o*-cresol hydrogenation has many advantages such as simpler process, lower toxicity, and higher yield of target products [7]. Therefore, the hydrogenation of *o*-cresol is recognized as a relatively promising strategy to produce *o*-methyl cyclohexanol [8]. The reaction is classified into gas-phase hydrogenation and liquid-phase hydrogenation. In comparison with the former, the latter has mild reaction conditions and better heat transfer, attracting wide attention [9].

To date, a large number of studies have been devoted to the catalytic hydrogenation of cresols. Early, single- or multi-component sulfide catalysts with Ni, Co, and Mo as active components are mainly used [10–12], but their practical application is hampered by the easy deactivation of the catalysts and the contamination of the products due to the leaching of the sulfurizing agent [13]. In contrast, precious metal catalysts, especially Pt [14, 15], Pd [16–18], and Ru [19], show favorable catalytic activity and selectivity for the target products. However, the shortcomings of precious metals, such as limited resources, expensive costs and environmental hazards of lost metals, limit their application. The development of widely available and low-cost non-precious metal catalysts is believed to be an effective and promising strategy. Unfortunately, non-precious metals are poorly active for hydrogenation at low temperatures, while high temperatures induce metal particles sintering and deactivation [20]. Hence, it is important to design environmentally friendly, highly active, selective, and stable non-precious metal catalysts for the hydrogenation of cresols.

Metal–organic frameworks (MOFs) composed of metal ions and organic ligands are of wide interest for their unique features such as high specific surface area, tunable pore size, highly ordered structure, and ease of functionalization [21], which facilitate the growth of small and highly dispersed metal nanoparticles on nitrogen-doped carbon during high-temperature pyrolysis [22]. Hollow structural materials are beneficial for shortening the diffusion path of reactants owing to their unique cavities and thinner shell layers [23], and protecting the encapsulated active metal nanoparticles from aggregation, sintering and leaching, thereby improving the catalytic activity and stability of the catalysts. The combination of hollow structures with nitrogen-doped carbon has been proposed as an ideal carrier for active metal components [24].

Recently, it has been reported that Co-based catalysts exhibit good activity and selectivity for cyclohexanol in the hydrogenation of phenolic compounds. For example, Wei et al. [25] obtained cobalt oxide nanoparticles loaded on porous carbon (CoO_x@CN) by direct pyrolysis of d-glucosamine hydrochloride, melamine and $CoCl_2 \cdot 6H_2O$, which could efficiently and selectively hydrogenate phenol to cyclohexanol with a 98% of yield. Li et al. [26] synthesized Co–Ni alloy nanoparticles embedded in nitrogen-doped carbon based on the MOF template strategy for the phenol hydrogenation, achieving the first reported case of cyclohexanol as the only product.

Here, we reported the synthesis of hollow-structured nitrogen-doped carbon encapsulated with Co nanoparticles (Co@HCN) by one-step high-temperature pyrolysis of hollow ZIF-67 (HZIF-67) under argon atmosphere. HZIF-67 was obtained by a single-solvent liquid–liquid interface method according to our previous work [27]. The effects of the pyrolysis temperature and $Co(NO_3)_2 \cdot 6H_2O$ concentration on the microstructures and catalytic performance of the Co@HCN catalysts for the selective hydrogenation of *o*-cresol to *o*-methyl cyclohexanol were investigated in detail. Although MOF-derived materials are not scarce in the field of catalysis [28–30], the hollow-structured MOF-derived non-precious metal catalysts we developed are applied for the first time to the reaction system of selective hydrogenation of *o*-cresol to *o*-methyl cyclohexanol.

2 Experimental

The chemicals utilized to fabricate catalysts and analyze catalytic capabilities were not required to be further purified, as detailed in the Supporting Information.

2.1 Synthesis of Co@HCN Catalysts

The fabrication process of Co@HCN is shown in Scheme 1, which is mainly divided into the following two steps: synthesis of HZIF-67 and its one-step pyrolysis.

HZIF-67 nanospheres were prepared by a single-solvent liquid–liquid interface method previously reported by our group [27]. The octanol was chosen as the solvent due to its poor water solubility to build two-phase interfaces with the hydration water of cobalt nitrate hexahydrate to form ZIF-67 with well-defined hollow structure [27, 31]. 2-Methylimidazole (2-MeIM, 0.24 mol) was completely dissolved in 200 mL of octanol with magnetic stirring at

Scheme 1 Schematic diagram of Co@HCN synthesis
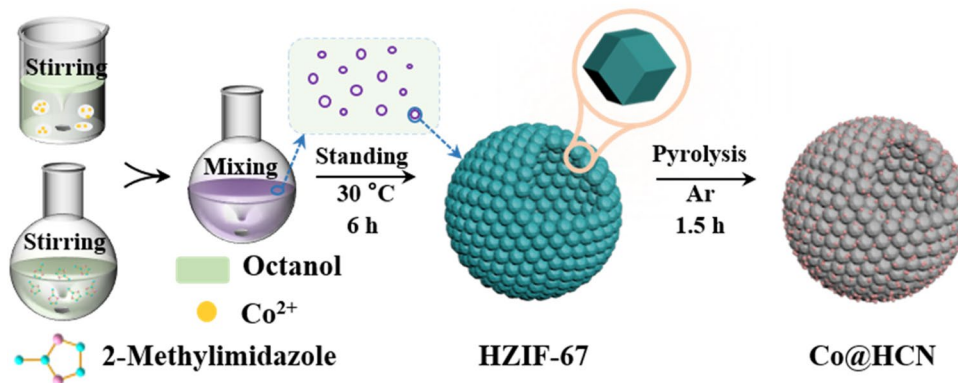
30 °C for 15 min, marked as solution A. A certain amount of $Co(NO_3)_2 \cdot 6H_2O$ was added to octanol (40 mL) and entirely dissolved after magnetic stirring at 30 °C for 15 min, marked as solution B. While the solution A was stirred, the solution B was quickly poured into it to obtain a mixed solution, which was stirred for 5 min. After standing in a 30 °C water bath for 6 h (Scheme 1), the samples were centrifuged, washed with methanol five times and dried at 70 °C overnight after standing in a 30 °C water bath for 6 h, and then weighed to obtain the yield of HZIF-67. A series of HZIF-67 nanospheres were obtained by varying the amount of $Co(NO_3)_2 \cdot 6H_2O$, labeled as HZIF-67-x, where x (x = 0.05, 0.1, 0.2, 0.3, 0.4 mol L^{-1}) represents the $Co(NO_3)_2 \cdot 6H_2O$ concentration in the solution B.

The black product was gained by calcining 0.9 g of the as-prepared HZIF-67 in a high-temperature tube furnace under argon atmosphere (40 mL min^{-1}), marked as Co@HCN-T-x (T = 450, 485, 500, 600, 700 °C; x = 0.05, 0.1, 0.2, 0.3, 0.4 mol L^{-1}), where T represents the pyrolysis temperature and x represents the $Co(NO_3)_2 \cdot 6H_2O$ concentration. The specific heating procedure was as follows. The temperature was increased from room temperature to 450 °C at a heating rate of 5 °C min^{-1}, held for 90 min, and then further increased to the target temperature at 2 °C min^{-1} for 90 min.

2.2 Evaluation of Catalytic Performance

The catalytic performance of the prepared Co@HCN catalysts was evaluated by the reaction system of *o*-cresol hydrogenation to obtain *o*-methyl cyclohexanol. The *o*-cresol hydrogenation process was carried out in an autoclave with a 30 mL quartz-liner fitted with a pressure gauge and a magnetic stirring function. Typically, 10 mL of 0.5 wt.% *o*-cresol-cyclohexane solution and 50 mg of catalyst were loaded into the reactor. The autoclave was sealed, replaced several times with N_2 and charged with H_2 to 3.5 MPa. After the reactor jacket was preheated to 220 °C, the reactor was placed and the reaction mixture was stirred at 250 rpm for 2 h. After cooling and releasing the remaining gas, the

product was filtered and analyzed by gas chromatography (Shimadzu GC 2014).

Apart from *o*-cresol, the catalytic performance of phenol, *m*-cresol and *p*-cresol was compared over Co@HCN-500-0.1 and Co@HCN-500-0.4. Additionally, the recoverability and recyclability of the Co@HCN-500-0.1 catalyst for the hydrogenation of *o*-cresol were investigated. After each reaction, the catalyst was separated from the reaction solution through an external magnet, and washed several times with cyclohexane before proceeding to the next reaction.

3 Results and Discussion

3.1 Fabrication and Characterization of Co@HCN

HZIF-67-0.1 is achieved by a single-solvent-interfacial strategy [27]. The XRD pattern (Fig. 1a) shows that the diffraction peaks (blue) of the as-prepared sample match well with the simulated ZIF-67 standard spectral peaks (black), suggesting the formation of ZIF-67 nanocrystals. The morphology of nanospheres with a size of approximately 100–250 nm is observed in the FESEM image (Fig. 1b). The presence of cavities (orange circles) is identified from few broken spheres (Fig. 1b), which is further confirmed by TEM images (Fig. 1c, d). A careful observation of the outer surface of the nanospheres reveals that the shell layer is assembled from many nanoparticles. These results indicate the successful synthesis of well-defined hollow ZIF-67 nanospheres.

A series of Co@HCN-T-0.1 are achieved by the pyrolysis of HZIF-67-0.1 under the Ar flow in a tube furnace at different temperatures (450–700 °C). The FESEM images (Fig. 2a–e) exhibit that the as-prepared Co@HCN-T-0.1 catalysts well maintain the spherical morphology of HZIF-67-0.1 (Fig. 1b). The presence of nanotube filamentary structures on the nanosphere surface under high temperatures makes the appearance rougher (Fig. 2d, e). This is based on the role of Co particles formed during pyrolysis

Fig. 1 **a** XRD pattern, **b** FESEM image and **c**, **d** TEM images of HZIF-67-0.1
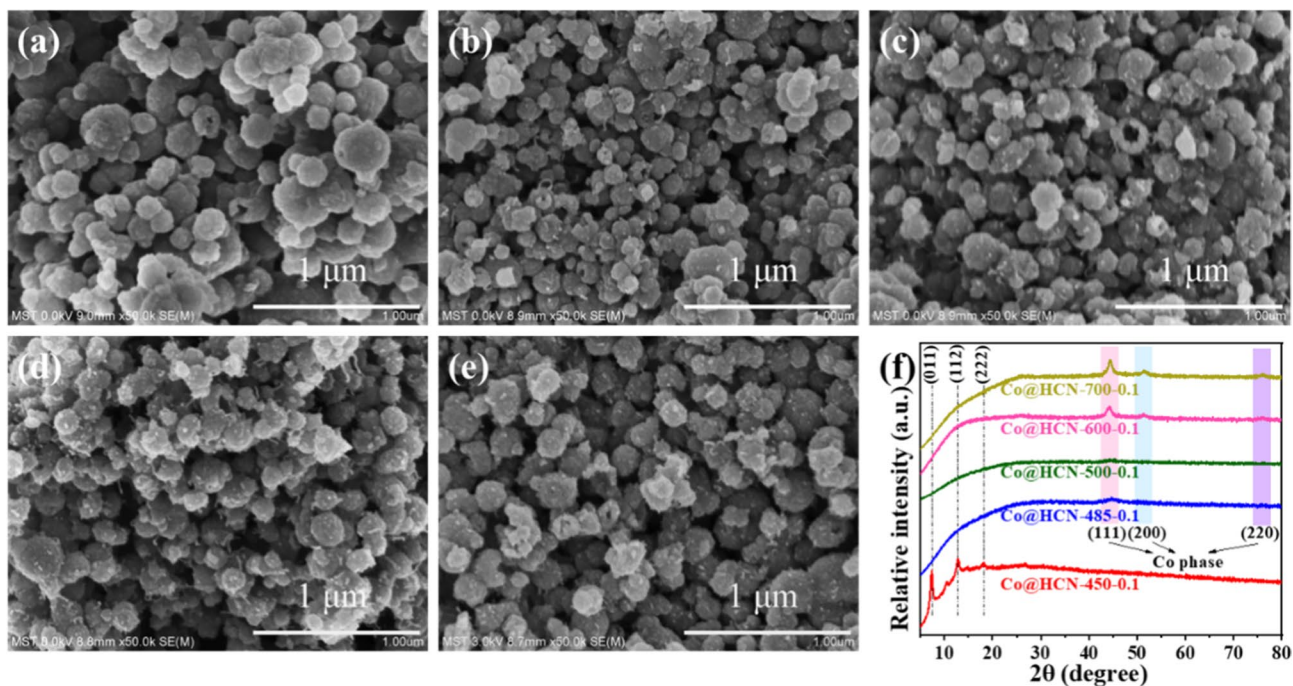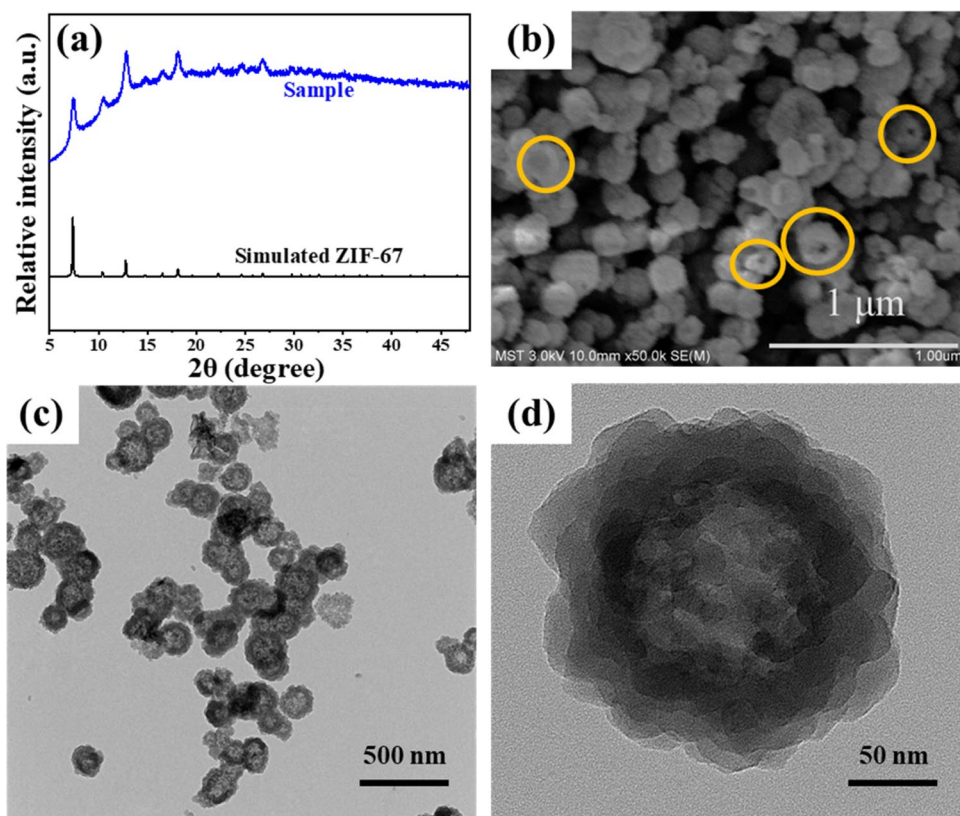

Fig. 2 **a–e** FESEM images and **f** XRD patterns of Co@HCN-T-0.1, T = (**a**) 450, (**b**) 485, (**c**) 500, (**d**) 600, (**e**) 700 °C

by catalyzing the formation and growth of carbon nanotubes [32]. Some characteristic peaks of HZIF-67-0.1 are still retained in Co@HCN-450-0.1 (Fig. 2f), illustrating that the ZIF framework is not entirely pyrolyzed at 450 °C. For other Co@HCN-T-0.1 samples, the peaks at 44.3°, 51.8°, and 76.0° are indexed to the (111), (200), and (220) planes

in the order, reflecting the formation of the face-centered cubic metallic Co (JCPDS No. 15-0806) [33] at 485, 500, 600, and 700 °C. Therefore, a suitable pyrolysis temperature is a critical factor for converting HZIF-67 into the required Co@HCN catalyst. It is evident that the Co phase peaks become sharper and more intense with increasing the pyrolysis temperature from 485 to 700 °C, manifesting that the Co@HCN catalysts obtained by high pyrolysis temperature possess cobalt particles with large size and high crystallization [34]. The degree of graphitization is not enough that the peaks of graphite C for all catalysts are undetectable.

The Raman spectra of the typical catalysts clearly exhibit two peaks at 1330 and 1580 cm^{-1} (Fig. S1), which are attributed to the disordered sp^3-C (D band) and graphite sp^2-C (G band), respectively. The strength ratio between the D and G bands (I_D/I_G) decreases and then increases with increasing pyrolysis temperature, which shows that the suitable pyrolysis temperature improves the graphitization degree. The carbonized graphite shell confers good electron transfer ability to the Co@HCN-500-0.1 catalyst [35]. In addition, the distinct peaks at 465, 509 and 671 cm^{-1} corresponding to the Co particles [36] can be observed, which is consistent with the XRD results (Fig. 2f).

The TEM results of the typical Co@HCN-T-0.1 catalysts are given in Fig. 3 to further evaluate their morphology and microstructure. The size of Co@HCN-T-0.1 (T = 450, 500, 700 °C) decreases with increasing pyrolysis temperature owing to the more loss of organic components and structural shrinkage during high temperature pyrolysis (Fig. 3a-1, b-1 and c-1). Interestingly, all these materials retain the original internal cavities, indicating that stable hollow spheres do not collapse during the pyrolysis process. The lattice stripes of d = 0.21 nm and d = 0.34 nm in the HRTEM images belong to the Co(111) and C(002) planes, respectively. Because HZIF-67-0.1 is not fully pyrolyzed at 450 °C, no clear graphitic carbon fringes are observed (Fig. 3a-2). As depicted in Fig. 3a-4, b-4 and c-4, the average particle size of Co nanoparticles increases from 3.0 to 7.7 nm with increasing pyrolysis temperature, indicating that higher pyrolysis temperature is not conducive to the fabrication of Co nanoparticles with small particle size. The larger size of nanoparticles is a result of the aggregated growth of Co particles through a combination of adjacent Co species [34]. The presence of large quantities of Co particles promotes the random growth of carbon nanotubes on the catalyst surface at high pyrolysis temperatures, which is in accordance with the FESEM results (Fig. 2). The mapping images show that C, N, and O elements are uniformly distributed in the shell of the catalysts (Fig. 3a-3, b-3 and c-3). The aggregation of Co nanoparticles results in the uneven distribution of Co element at high pyrolysis temperatures, especially at 700 °C (Fig. 3c-3). By comparison, it is seen that the Co nanoparticles with relatively high crystallinity (Figs. 2f and 3b-2), relatively small

size (Fig. 3b-4) and homogeneous distribution (Fig. 3b-1 and b-3) can be developed at suitable pyrolysis temperature, and they can be effectively protected by the N, O-doped carbon matrix (Fig. 3b-3).

Co@HCN-450-0.1 shows a type-I isotherm (Fig. S2A), demonstrating its predominant microporous structure. In contrast, Co@HCN-500-0.1, Co@HCN-600-0.1 and Co@HCN-700-0.1 all express type-IV isotherms. Similarly, H3-type hysteresis loops are observed for all catalysts at relative pressures between 0.5 and 1.0 (Fig. S2A), confirming the presence of meso-/macro-porous pores, which are attributed to particle stacking interstices and hollow cavities. As shown in Fig. S2B, with regard to all catalysts, the pore size is mainly distributed in the range of 1–20 nm, and the prominent peak at 4 nm is probably from the interstices of adjacent nanoparticles in the shell layer [27], which is speculatively consistent with the FESEM images (Fig. 2a–e) showing that all of them are nanospheres assembled by particles. Table 1 displays the specific surface area and pore structure information of the catalysts. The largest specific surface area (967.5 m^2 g^{-1}) and pore volume (0.75 cm^3 g^{-1}) of Co@HCN-450-0.1 are due to the fact that HZIF-67 is not entirely carbonized at 450 °C and still retains its original structural properties (Fig. 2f). When the temperature increases from 450 to 500 °C, the specific surface area and pore volume decrease sharply attributed to the collapse and combination of micropores [37]. Due to the decomposition of organic ligands, the gradual formation of completely open skeleton makes the specific surface area and pore volume show an increasing trend with further increase in the pyrolysis temperature. Notably, Co@HCN-500-0.1 displays the highest percentage of meso-/macro-porous specific surface area and pore volume, which facilitates the diffusion of substrate molecules and thus may increase the catalytic activity.

The XPS survey spectra reveal that the catalyst surface contains C, N, O and Co elements (Fig. 4), in line with the TEM results (Fig. 3a-3, b-3 and c-3). The Co content on the catalyst surface tends to increase and then decrease as the pyrolysis temperature increases (Table 2). Although the total Co content of Co@HCN-500-0.1 is not the highest (Table S1), it has the highest surface Co content (5.03 at.%), which can be explained by the alteration of structural composition through calcination and uniformly dispersed Co particles (Fig. 3b-3). The presence of a broader number of easily accessible active sites in Co@HCN-500-0.1 improves the utilization of active sites and is of critical significance for the enhancement of catalytic activity. With increasing pyrolysis temperature, the surface N content shows the same trend. The pyrolysis of HZIF-67 at low temperatures promotes the formation of stable metal nitride [38], resulting in well-retained N element and an increase in the surface N content. The release of N in the form of N_2 and/or NH_3 at high temperatures makes the surface N content
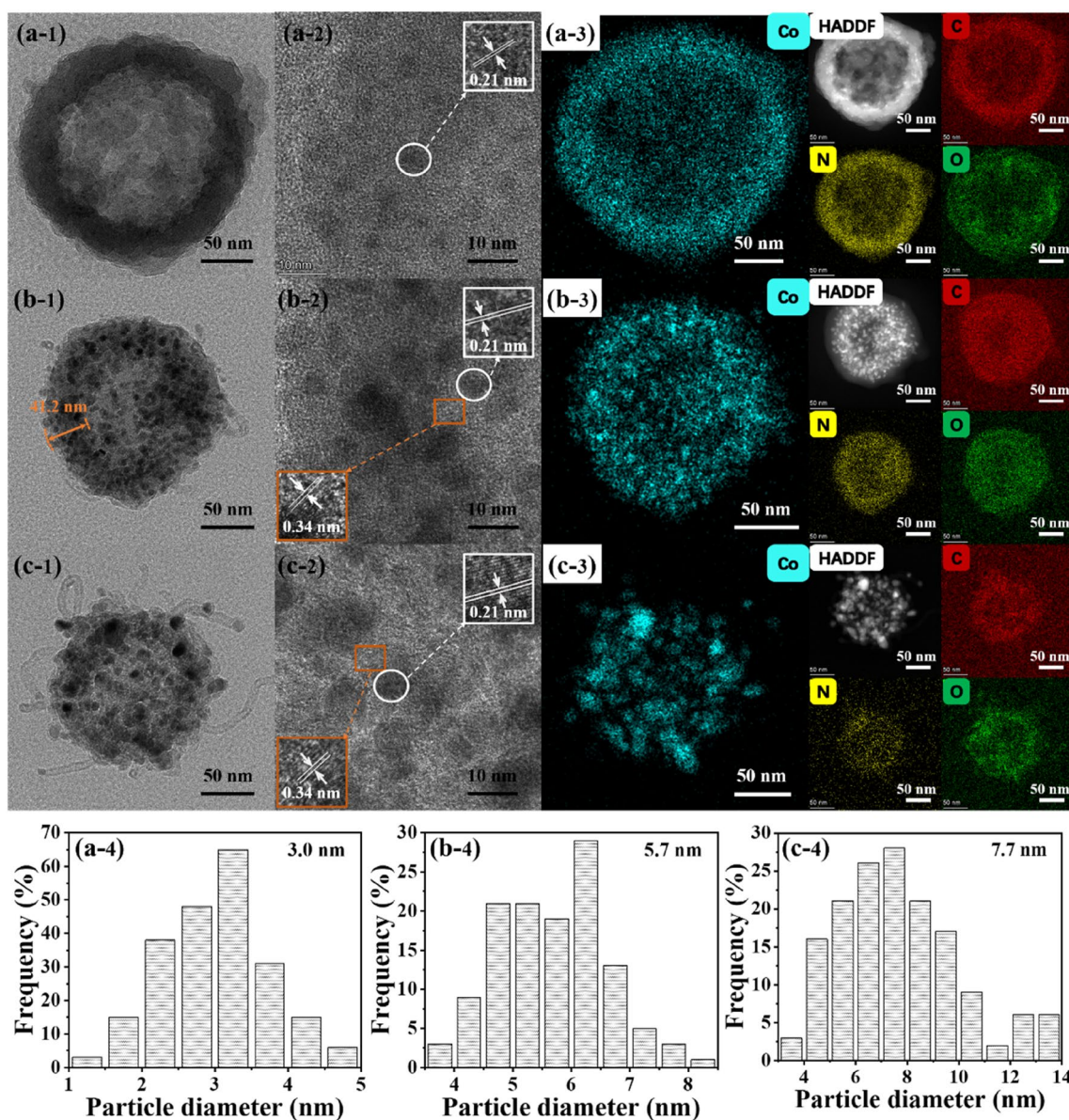
Fig. 3 TEM images of (a-1, a-2) Co@HCN-450-0.1, (b-1, b-2) Co@HCN-500-0.1, (c-1, c-2) Co@HCN-700-0.1; HAADF and elemental mapping images of (a-3) Co@HCN-450-0.1, (b-3) Co@HCN-500-0.1, (c-3) Co@HCN-700-0.1; size distribution of Co nanoparticles in (a-4) Co@HCN-450-0.1, (b-4) Co@HCN-500-0.1, (c-4) Co@HCN-700-0.1

Table 1 Textural properties of the Co@HCN catalysts

Samples	S_{BET} (m^2 g^{-1})	S_{extra}/S_{BET}	V_{total} (cm^3 g^{-1})	V_{extra}/V_{total}
Co@HCN-450-0.1	967.5	0.20	0.75	0.57
Co@HCN-500-0.1	79.4	0.72	0.23	0.96
Co@HCN-600-0.1	212.6	0.40	0.31	0.84
Co@HCN-700-0.1	252.0	0.43	0.37	0.84
Co@HCN-500-0.4	56.1	0.73	0.16	0.96

reduce [39]. Figure 5 shows the deconvolution of the Co $2p_{3/2}$ regions of Co@HCN-T-0.1, which is consisted of metal Co° (778.2 eV), Co–O (780.7 eV), CoN$_x$ (782.5 eV) [40] and satellite peaks (786.3 eV) [41]. The appearance of Co–O is ascribed to the partial oxidation of the catalyst surface exposed to air [42]. The existence of CoN$_x$ is further
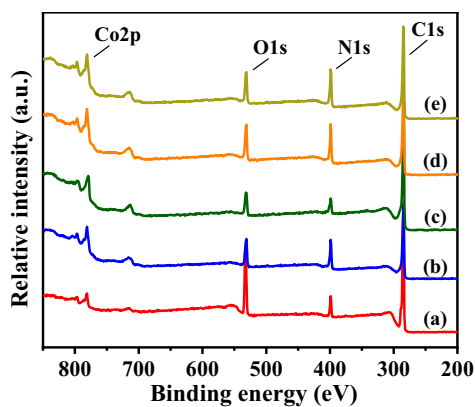
Fig. 4 XPS survey spectra of a Co@HCN-450-0.1, b Co@HCN-500-0.1, c Co@HCN-700-0.1, d Co@HCN-500-0.05 and e Co@HCN-500-0.4

Table 2 Elemental content on the surface of the Co@HCN catalysts

Samples	C 1s (at.%)	N 1s (at.%)	O 1s (at.%)	Co 2p (at.%)
Co@HCN-450-0.1	72.20	7.39	18.51	1.90
Co@HCN-500-0.1	65.69	17.45	11.84	5.03
Co@HCN-700-0.1	80.18	8.36	8.20	3.25
Co@HCN-500-0.05	65.35	17.40	12.12	5.13
Co@HCN-500-0.4	66.21	17.66	11.15	4.98

evidenced by the N 1s spectra (Fig. 5B). The CoN$_x$ content first increases and then decreases when the pyrolysis temperature rises from 450 to 700 °C (Fig. 5A, D). Co@HCN-500-0.1 exhibits maximum CoN$_x$ content of 30.8% (Fig. 5A). The Co° content increases from 0.8% to 17.7% with the rise in the pyrolysis temperature (Fig. 5A). This can be explained by that the decomposition of volatile components at high temperatures promotes the conversion of more CoN$_x$ to Co° [43]. Four different types of N are observed in the N 1s spectra of Co@HCN-T-0.1 (Fig. 5B), namely pyridinic-N (398.4 eV), CoN$_x$ (399.1 eV) [44–46], pyrrolic-N (400.1 eV) and graphitic-N (401.1 eV), which further prove that N species are successfully embedded in the carbon matrix. Partial N species combine with Co species to form the CoN$_x$ sites. The strong interaction between Co and π-electrons from sp^2 hybridization makes Co preferentially aggregate on sp^2-type N sites for nucleation and growth [47], which can stabilize the metal [48] and thus enhance the activity of the catalyst [38]. The high N content of Co@HCN-500-0.1 leads to a massive amount of CoN$_x$ on its surface (Fig. 5A, D; Table 2), which facilitates the

immobilization of Co in the catalyst and reduces the particle aggregation (Fig. 3b-3). In the cases of Co@HCN-T-0.1, the relative content of pyridinic-N gradually decreases with increasing pyrolysis temperature, while the contents of pyrrolic-N and graphitic-N increase (Fig. 5C). It is a result of the conversion of pyridinic-N, which has a weak thermal stability, to pyrrolic-N and graphitic-N at high temperatures [49]. Three fitting peaks at 284.8 eV, 285.8 eV and 289.1 eV observed in the C 1 s spectra (Fig. S3A) belong to the C–C, C–N and C–O bonds [50], respectively. The C elements on the sample surface are mainly in the form of C–C bond derived from the pyrolysis of 2-MeIM. The XPS spectra of O 1s (Fig. S3B) mainly contains three peaks, which are ascribed to Co–O bond (529.8 eV) [51], C–O bond (531.5 eV) [52] and physical and chemical adsorption of water on the surface (532.5 eV) [51].

The strength and density of the catalytic acidic sites influence the catalytic activity and product distribution [53]. Figure S4a shows the NH$_3$-TPD curves of Co@HCN-450-0.1, Co@HCN-500-0.1 and Co@HCN-700-0.1. The apparent upward trend of the NH$_3$-TPD curves of Co@HCN-450-0.1 and Co@HCN-500-0.1 after 400 °C is caused by the thermal decomposition of the carbon materials at high temperatures [54], as further verified by the TG characterization (Fig. S4b). The desorption peaks of Co@HCN-450-0.1 and Co@HCN-700-0.1 are relatively insignificant. In contrast, some enriched desorption peaks for Co@HCN-500-0.1 in the range of 100–400 °C are observed. The weight loss of this catalyst at low temperatures (Fig. S4b) may occupy parts of the desorption peaks. Wang et al. [55] reported that acid-catalyzed alcohol dehydration is the limiting step in the cresol hydrodeoxygenation and higher levels of acidic sites on the catalyst improve the reaction rate of alcohol dehydration. It can be speculated that the lower intensity and insufficient content of acid sites on the prepared Co@HCN-T-0.1 catalysts effectively limit the dehydration of o-methyl cyclohexanol and improve the selectivity of o-methyl cyclohexanol.

Furthermore, the influence of the Co(NO$_3$)$_2$·6H$_2$O concentration on the microstructures of Co@HCN-500 is discussed. When the Co(NO$_3$)$_2$·6H$_2$O concentration increases from 0.05 to 0.3 mol L^{-1}, the uniformity of HZIF-67 nanospheres worsens (Fig. S5a–d). HZIF-67-0.4 is overwhelmingly unassembled particles and consists of merely a few spheres (Fig. S5e). Higher Co(NO$_3$)$_2$·6H$_2$O concentration increases the crystallinity and yield of HZIF-67 defined by the mass after drying (Fig. S5f; Table S2) [56]. At the Co(NO$_3$)$_2$·6H$_2$O concentrations of 0.05–0.3 mol L^{-1}, the obtained Co@HCN-500 materials have similar morphology with HZIF-67 (Fig. S5g–j). Co@HCN-500-0.4 exhibits irregular and large blocks with clear agglomeration (Fig. S5k), due to the easy aggregation of small particles under high temperature pyrolysis (Fig. S5e). The Co crystallinity in Co@HCN-500 decreases with increasing Co(NO$_3$)$_2$·6H$_2$O
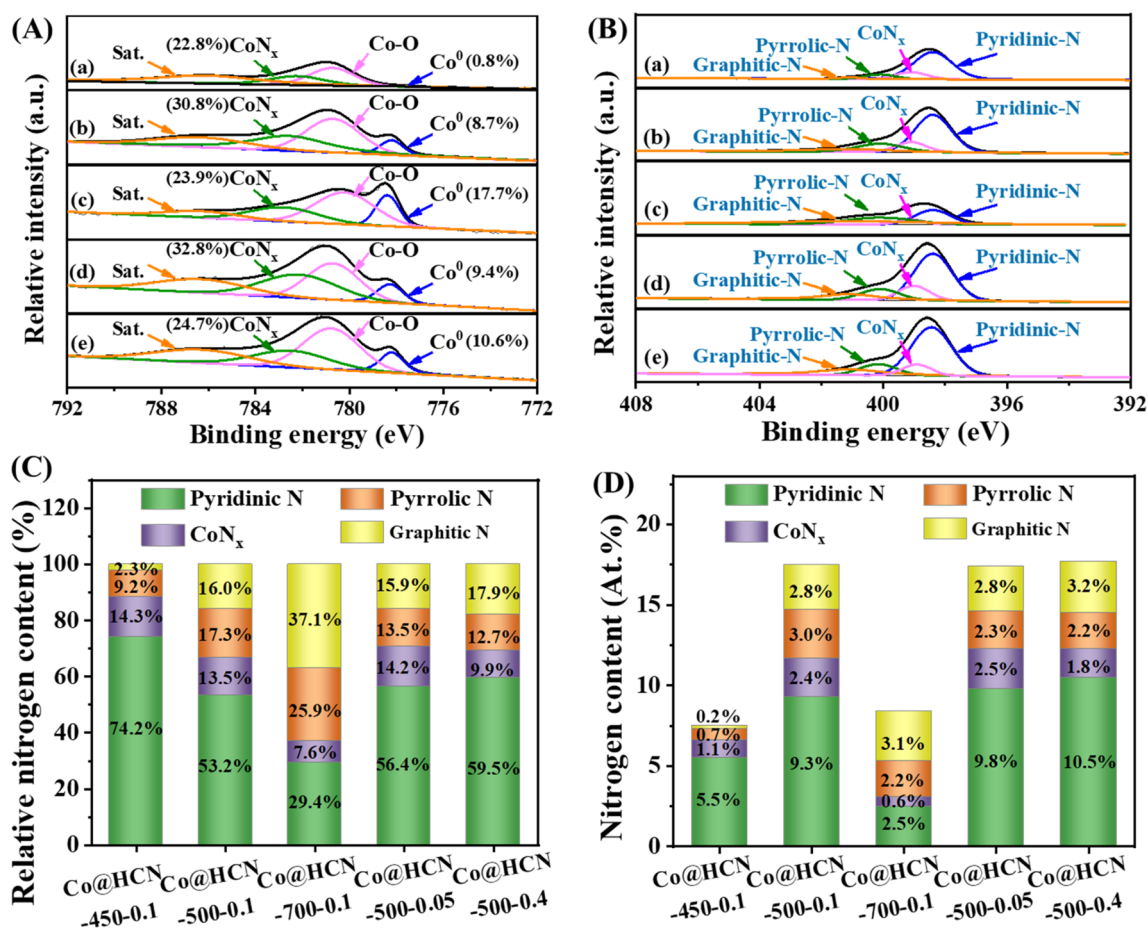
Fig. 5 **A** Co $2p_{3/2}$ and **B** N $1s$ spectra of (a) Co@HCN-450-0.1, (b) Co@HCN-500-0.1, (c) Co@HCN-700-0.1, (d) Co@HCN-500-0.05 and (e) Co@HCN-500-0.4; **C** relative content and **D** content of each N-specie

concentration (Fig. S5l). The Co(NO$_3$)$_2$·6H$_2$O concentration has no obvious influence on the surface defects of Co@HCN-500 (Fig. S1).

With increasing Co(NO$_3$)$_2$·6H$_2$O concentration, the catalyst shifts from hollow to solid (Figs. 3b-1 and 4). Lower Co(NO$_3$)$_2$·6H$_2$O concentration limits the nucleation and growth of ZIF-67 to gain a thinner shell layer (Fig. 6a-1), while higher Co(NO$_3$)$_2$·6H$_2$O concentration promotes the nucleation and growth of ZIF-67, resulting in the formation of solid catalyst (Fig. 6b-1) [57]. Higher Co(NO$_3$)$_2$·6H$_2$O concentration is in favor of the combination of adjacent Co species [58], leading to larger particle size of Co nanoparticles (Figs. 4a-3, 3b-4, and 4b-3). The solid structure of Co@HCN-500-0.4 results in the apparently reduced hysteresis loop in the N$_2$ sorption isotherms (Fig. S2A), the disappearance of the peak at 4 nm in the pore size distribution curve (Fig. S2B), and the lower specific surface area and pore volume (Table 1). The Co(NO$_3$)$_2$·6H$_2$O concentration has no significant effect on the surface N content and total Co content (Tables 2 and S1). The surface contents of Co and CoN$_x$ reduce with an increase in the Co(NO$_3$)$_2$·6H$_2$O

concentration (Fig. 5A; Table 2), indicating that the thinner shell layer in hollow nanospheres is in favor of the exposure of Co species.

3.2 *o*-Cresol Hydrogenation Over Co@HCN

The catalytic performance of the Co@HCN catalysts was assessed by the hydrogenation of *o*-cresol to *o*-methyl cyclohexanol. For comparison, the blank test without any catalyst and the catalytic performance of HZIF-67 were also investigated. Almost no hydrogenation occurs for the two controlled experiments. Instead, an excellent *o*-cresol hydrogenation performance is achieved by the as-prepared Co@HCN catalysts (Fig. 7), confirming the necessity of catalysts and the pyrolysis of HZIF-67 for the *o*-cresol hydrogenation. In all cases, the selectivity of *o*-methyl cyclohexanol is above 99% (Fig. 7), and only a trace amount of *o*-methyl cyclohexanone is detected, which may be attributed to the weaker acidity of the catalysts (Fig. S4a). Both preparation parameters and reaction conditions significantly influence the catalytic activity (Fig. 7). With increasing pyrolysis
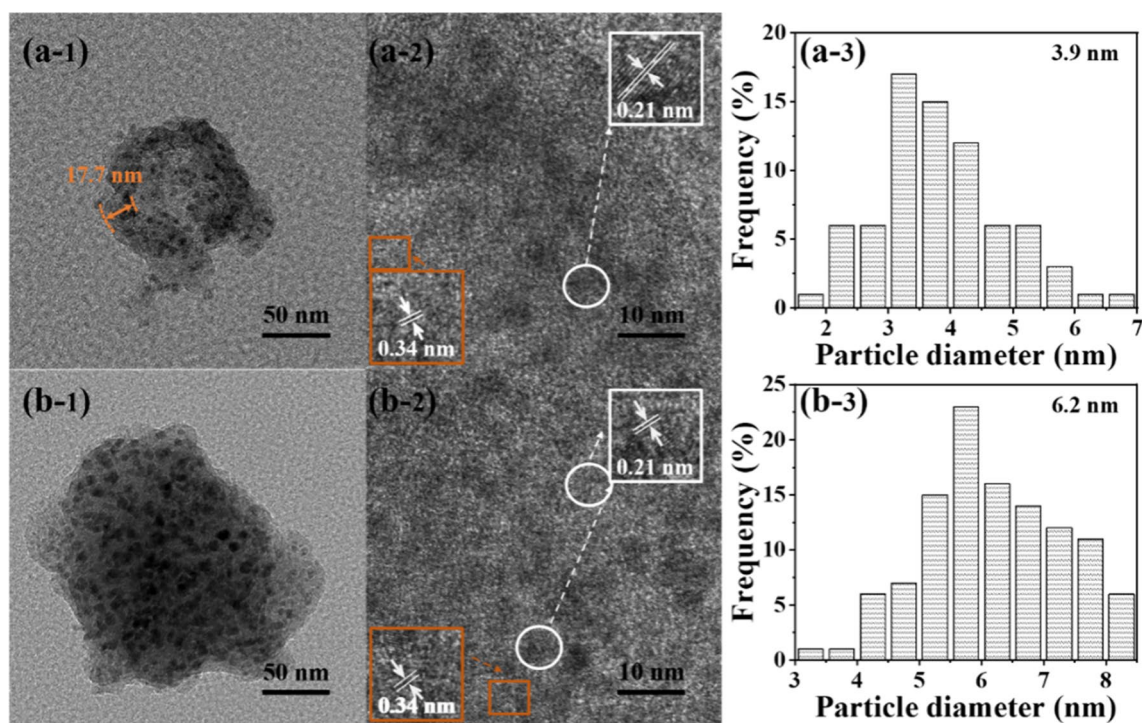
Fig. 6 TEM images of (a-1, a-2) Co@HCN-500-0.05 and (b-1, b-2) Co@HCN-500-0.4; size distribution of Co nanoparticles in (a-3) Co@HCN-500-0.05 and (b-3) Co@HCN-500-0.4

temperature, the *o*-cresol conversion of Co@HCN-T-0.1 exhibits a typical volcano-type curve. For Co@HCN-450-0.1, the conversion of *o*-cresol is 58.3%. The catalytic activity of Co@HCN-500-0.1 is significantly enhanced with an *o*-cresol conversion of 94.4% and an *o*-methyl cyclohexanol yield of 94.0% (Fig. 7a). With further increase in the pyrolysis temperature, the yield of *o*-methyl cyclohexanol for the Co@HCN-700-0.1 catalyst is only 53.7%. Among them, Co@HCN-500-0.1 performs the best catalytic activity for the following reasons. Firstly, Co@HCN-500-0.1 possesses the maximum ratio of meso-/macro-pore specific surface area and pore volume (Table 1), facilitating the diffusion of reaction substrates. Secondly, the highest surface Co content of Co@HCN-500-0.1 (Table 2) supplies more accessible active sites and promotes the dissociation of H_2 into active H atoms [59]. Thirdly, the higher CoN_x content (Fig. 5A, D) plays an important role in the immobilization and dispersion of Co species to obtain Co nanoparticles with small particle size and uniform dispersion (Fig. 3b-1, b-3 and b-4), allowing them to show efficient catalytic performance in catalytic reactions. These aspects together contribute to the superior catalytic activity of Co@HCN-500-0.1. Co@HCN-450-0.1 owns the best Co distribution (Fig. 3a-3), the smallest Co size (Fig. 3a-4), and the highest specific surface area and pore volume (Fig. S2A, Table 1), but its lowest total Co content (Table S1), surface Co content (Table 2), and surface Co° content (Fig. 5A) lead to the lower catalytic activity

(Fig. 7a). The worst Co distribution (Fig. 3c-3) and the largest Co size (Fig. 3c-4) should be the main reasons for the lowest catalytic activity of Co@HCN-700-0.1 (Fig. 7a).

The influence of the $Co(NO_3)_2 \cdot 6H_2O$ concentration on the catalytic activity of Co@HCN-500 was investigated (Fig. 7b). Surprisingly, the catalyst activity decreases with increasing $Co(NO_3)_2 \cdot 6H_2O$ concentration. For Co@HCN-500-0.05, the *o*-cresol conversion is as high as 87.0% after just 1 h of reaction. In contrast, Co@HCN-500-0.4 only achieves an *o*-cresol conversion of 55.8%. The superior catalytic activity of Co@HCN-500-0.05 is closely related to its hollow structures. On one hand, a limited number of nucleation sites are formed at low $Co(NO_3)_2 \cdot 6H_2O$ concentration and the growth of ZIF-67 is restricted, allowing the Co@HCN-500-0.05 catalyst to behave as hollow nanospheres with a thin shell layer and small size (Fig. 6a-1), which have a positive effect on the formation of Co nanoparticles with high crystallinity (Fig. S5l), small average particle size (Fig. 6a-3), and better dispersion (Fig. 6a-1). On the other hand, the thinner shell layer in hollow nanospheres is in favor of the exposure of Co species (Fig. 5A; Table 2), improving the utilization of the active component. Although Co@HCN-500-0.05 exhibits the optimal catalytic activity, the lower yield (Table S2) greatly increases the preparation cost, which is not conducive to scale-up applications. Higher $Co(NO_3)_2 \cdot 6H_2O$ concentration of 0.4 mol L^{-1} results in the formation of solid Co@HCN-500-0.4 (Fig. 6b-1) with

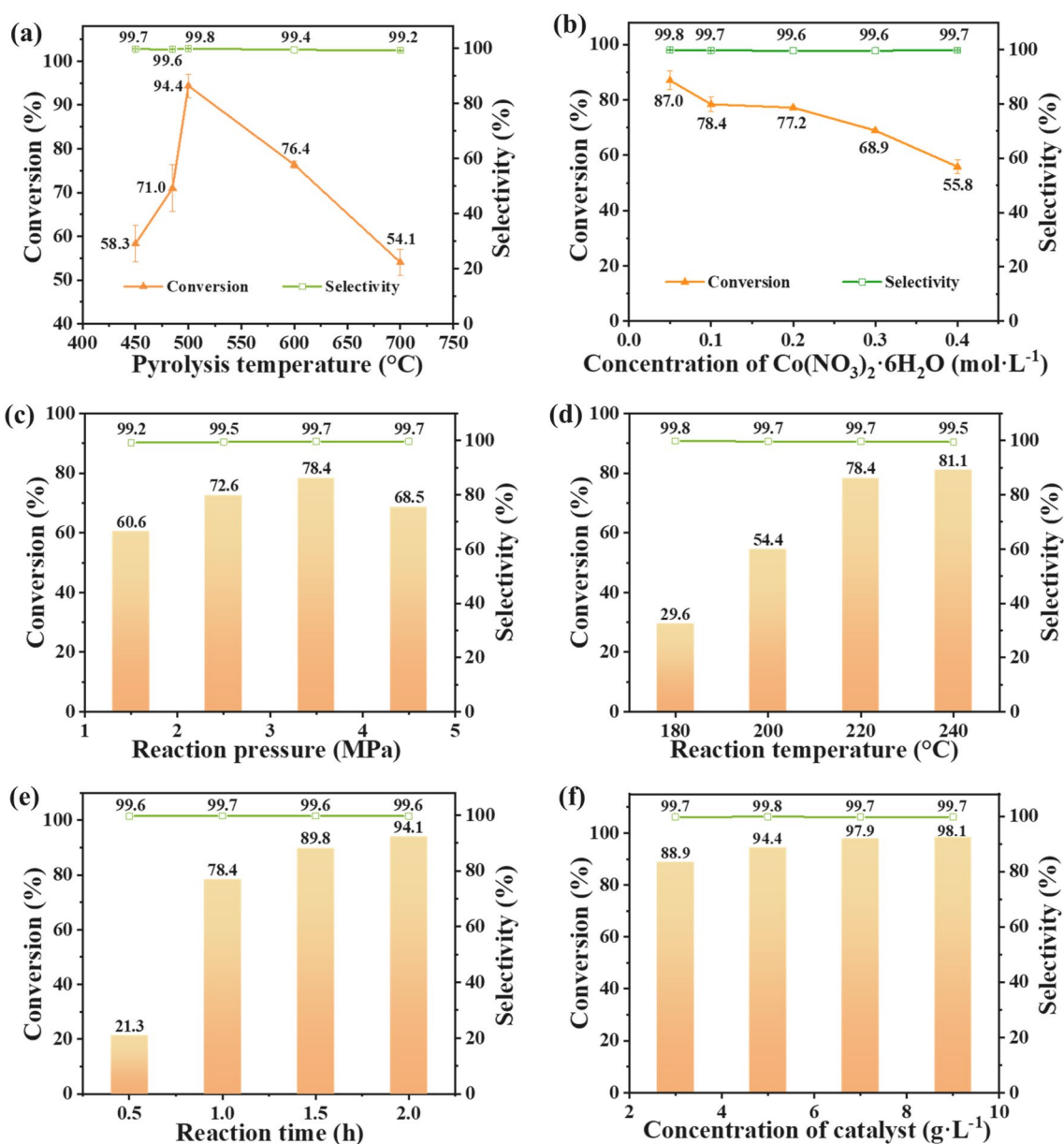**Fig. 7** Catalytic performance of Co@HCN varied with **a** pyrolysis temperature (reaction time: 2 h), **b** Co(NO$_3$)$_2$·6H$_2$O concentration, **c** reaction pressure, **d** reaction temperature, **e** reaction time and **f** catalyst concentration (reaction time: 2 h). Unless otherwise stated, the reaction conditions were as follows: 10 mL of 0.5 wt.% *o*-cresol-cyclohexane solution, catalyst concentration 5 g L^{-1}, 3.5 MPa H$_2$, 220 °C, 1 h

larger particle size of Co nanoparticles (Fig. 6b-3), lower specific surface area and pore volume (Table 1), and lower surface contents of Co and CoN$_x$ (Fig. 5A, Table 2), thereby decreasing the catalytic activity (Fig. 7b). According to the above analyses, the suitable Co(NO$_3$)$_2$·6H$_2$O concentration is 0.1 mol L^{-1}.

The reaction pressure, reaction temperature, reaction time and catalyst concentration are important factors influencing the catalytic performance of catalysts, and their effects on the hydrogenation performance of *o*-cresol over Co@ HCN-500-0.1 were investigated (Fig. 7c–f). The *o*-cresol conversion first increases and then decreases with increasing H$_2$ pressure. Too high pressure may cause catalyst deactivation [60], decreasing the reaction rate and o-cresol conversion. The optimal reaction pressure is 3.5 MPa. As expected, a high reaction temperature is in favor of promoting the hydrogenation reaction (Fig. 7d). Considering the energy consumption, 220 °C is chosen as the optimal temperature. The reaction time exhibits the same trend, and the *o*-cresol conversion reaches 94.1% at 2 h. As the catalyst

concentration rises, the conversion increases. When the catalyst concentration increases from 7 to 9 g L^{-1}, the *o*-cresol conversion rises by only 0.3%. Thus, the catalyst concentration of 7 g L^{-1} is selected. Co@HCN-500-0.1 can achieve an *o*-cresol conversion of 97.9% and an *o*-methyl cyclohexanol selectivity of 99.7% at the reaction pressure of 3.5 MPa, reaction temperature of 220 °C, reaction time of 2 h, and catalyst concentration of 7 g L^{-1}.

The catalytic results of the as-prepared Co@HCN catalysts for the *o*-cresol hydrogenation to *o*-methyl cyclohexanol are compared to the representative non-precious metal catalysts in literature using the turnover frequency (TOF) as a technical indicator (Table S3). Co@HCN-500-0.1 achieves the highest TOF value among the Co@HCN catalysts, which is 3.3 times higher than Co@HCN-700-0.1 and 1.3 times higher than Co@HCN-500-0.4. Interestingly, Co@HCN-500-0.1 has a relatively high TOF value compared to the reported non-precious metal catalysts (Table S3). The better catalytic performance of Co@HCN-500-0.1 should be ascribed to its larger percentage of meso-/macro-pores (Table 1), dispersing small Co nanoparticles (Fig. 3b-1, b-3 and b-4), and abundant surface Co and CoN$_x$ contents (Fig. 5A; Table 2), which significantly enhance the mass transfer and increase the utilization of Co nanoparticles, favoring the selective hydrogenation of *o*-cresol (Fig. 8). The results indicate that the as-fabricated Co@HCN-500-0.1 catalyst is promising for the selective *o*-cresol hydrogenation.

Co@HCN-500-0.1 was chosen as a representative catalyst to evaluate the catalytic stability. The selectivity remains stable and the *o*-cresol conversion keeps at around 80% during 8 reaction cycles (Fig. 9a). The catalyst can be separated easily from the reaction mixture by a magnet owing to its magnetic properties (Fig. 9b). There are no significant changes in the crystal structure, N$_2$ sorption, morphology, size and Co particles of the recovered catalyst as compared to the fresh one (Fig. 9c-f). The ICP analysis of the reaction solution after the filtration of Co@HCN-500-0.1 indicate that there is no obvious Co leaching during 8 reaction cycles. The above results confirm the as-prepared Co@HCN-500-0.1 catalyst has good stability and reusability in the hydrogenation of *o*-cresol to *o*-methyl cyclohexanol.

Furthermore, Co@HCN-500-0.1 was tested in the hydrogenation of phenol, *m*- and *p*-cresol for evaluating its universality. To illustrate the advantages of the as-prepared HZIF-67-derived hollow structured Co-based carbon material, the catalytic performance of Co@HCN-500-0.4 was also tested. All these reactants can be converted to the corresponding alcohols with high selectivity (> 99%), which fully supports the wide applicability of the as-prepared Co@HCN catalysts in the hydrogenation of phenol and its derivatives. Notably, in all cases, Co@HCN-500-0.1 exhibits better catalytic activity than Co@HCN-500-0.4, which is related to the hollow interior, surface composition and Co particle size. The hollow interior of Co@HCN-500-0.1 (Fig. 3b-1) is more favorably for mass transfer [23]. The Co content on the surface of Co@HCN-500-0.1 is slightly higher than that of Co@HCN-500-0.4 (Table 2), which provides more active sites to facilitate the dissociation of H$_2$ into active H atoms [59]. In addition, the CoN$_x$ content on the surface of Co@HCN-500-0.1 is significantly higher than that of Co@HCN-500-0.4 (Fig. 5D), which greatly enhances the immobilization and dispersion of Co [48], so that Co nanoparticles with smaller particle size (Figs. 3b-4 and 6b-3) and more uniform dispersion (Figs. 3b-1 and 6b-1) are obtained. There are significant differences in the reactivity of phenol and its derivatives, mainly due to the differences in the steric and electronic effects [61] (Table 3).

4 Conclusion

Hollow Co@HCN nanospheres were synthesized by one-step pyrolysis of HZIF-67. The morphology, pore structure, Co size and distribution, surface composition, and yield of

Fig. 8 *o*-Methyl cyclohexanol synthesis by the *o*-cresol hydrogenation over Co@HCN-500-0.1
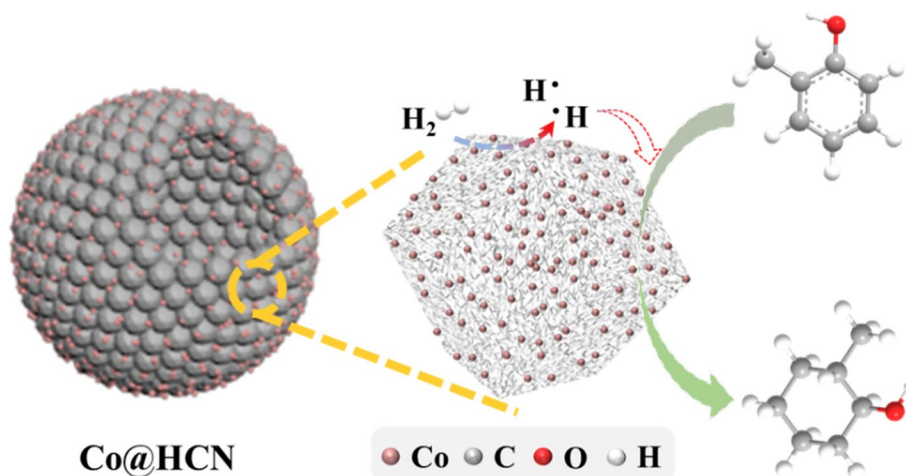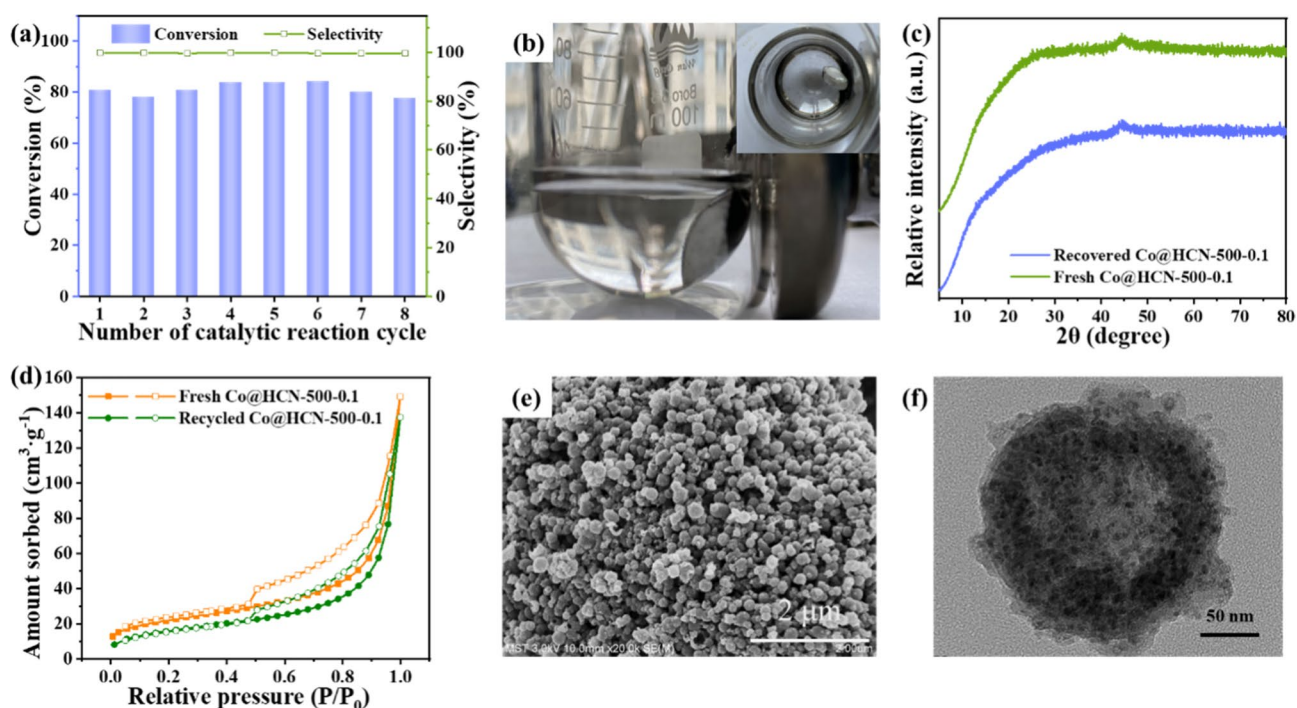
Fig. 9 **a** Recyclability investigation of Co@HCN-500-0.1 (reaction conditions: 10 mL of 0.5 wt.% o-cresol-cyclohexane solution, catalyst concentration 5 g L^{-1}, 3.5 MPa H$_2$, 220 °C, 1 h), **b** pictures of the catalyst during recycling, **c** XRD patterns, **d** N$_2$ sorption isotherms, **e** FESEM image and **f** TEM image of the Co@HCN-500-0.1 catalyst after 8 cycles

Table 3 Catalytic performance of the hydrogenation of phenol and its derivatives

Entry	Substrates	Products	Catalysts	Conversion	Selectivity
1			Co@HCN-500-0.1[a]	78.4%	99.7%
2			Co@HCN-500-0.4[a]	55.8%	99.7%
3			Co@HCN-500-0.1[b]	85.9%	99.4%
4			Co@HCN-500-0.4[b]	61.5%	99.4%
5			Co@HCN-500-0.1[b]	90.9%	99.6%
6			Co@HCN-500-0.4[b]	58.5%	99.5%
7			Co@HCN-500-0.1[c]	71.4%	99.6%
8			Co@HCN-500-0.4[c]	35.7%	99.3%

Reaction conditions: 10 mL of 0.5 wt.% reactant-cyclohexane solution, 3.5 MPa H$_2$, 220 °C, [a] catalyst concentration 5 g L^{-1}, 1 h; [b] catalyst concentration 3 g L^{-1}, 1 h; [c] catalyst concentration 3 g L^{-1}, 0.5 h.

the Co@HCN catalysts can be adjusted by the pyrolysis temperature and Co(NO$_3$)$_2$·6H$_2$O concentration. Co@HCN-500-0.1 with larger mesoporous ratio, smaller and uniformly dispersed Co particles, rich surface-exposed Co content, and relatively high CoN$_x$ content exhibits the superior catalytic performance, achieving an o-cresol conversion of 97.9% and an o-methyl cyclohexanol selectivity of 99.7% in only 2 h at 220 °C and 3.5 MPa. The N-doped carbon protects the Co nanoparticles from aggregating and leaching, thus providing fascinating stability. Therefore, it can be believed that this Co@HCN-500-0.1 catalyst holds some potential for the efficient synthesis of o-methyl cyclohexanol from o-cresol.

References

1. Fakhri Z, Azad MT (2021) A combined experimental, geometry optimization and molecular dynamic simulations study of the binary mixtures of *cis* and *trans* 2-methylcyclohexanol and aniline. J Chem Thermodyn 154:106322–106333

2. Yu ZQ, Wang Y, Sun ZC, Li X, Wang AJ, Camaioni DM, Lercher JA (2018) Ni_3P as a high-performance catalytic phase for the hydrodeoxygenation of phenolic compounds. Green Chem 20:609–619

3. Ramachandran PV, Drolet MP, Kulkarni AS (2016) A non-dissociative open-flask hydroboration with ammonia borane: ready synthesis of ammonia-trialkylboranes and aminodialkylboranes. Chem Commun 52:11897–11900

4. Padhi SK, Kaluzna IA, Buisson D, Azerad R, Stewart JD (2007) Reductions of cyclic β-keto esters by individual saccharomyces cerevisiae dehydrogenases and a chemo-enzymatic route to (1R,2S)-2-methyl-1-cyclohexanol. Tetrahedron Asymmetry 18:2133–2138

5. Heravi MM, Ghassemzadeh M (1999) Solvent free tetrahydropyranylation of alcohols and phenols over sulfuric acid adsorbed on silica gel. Synth Commun 29:1013–1016

6. Xu Y, Li YB, Wang CW, Wang CW, Ma LL, Wang TJ, Zhang XH, Zhang Q (2017) In-situ hydrogenation of model compounds and raw bio-oil over Ni/CMK-3 catalyst. Fuel Process Technol 161:226–231

7. Li YP, Liu ZM, Xue WH, Crossley SP, Jentoft FC, Wang SW (2017) Hydrogenation of *o*-cresol on platinum catalyst: catalytic experiments and first-principles calculations. Appl Surf Sci 393:212–220

8. Chen MY, Cui Y, Qian W, Peng QP, Wang JJ, Gong HH, Fang J, Dai S, Hou ZS (2020) Thermoregulated ionic liquid-stabilizing Ru/CoO nanocomposites for catalytic hydrogenation. Langmuir 36:11589–11599

9. Turáková M, Salmi T, Eränen K, Wärnå J, Murzin DY, Králik M (2015) Liquid phase hydrogenation of nitrobenzene. Appl Catal A-Gen 499:66–76

10. Wang WY, Zhang K, Li L, Wu K, Liu PL, Yang YQ (2014) Synthesis of highly active Co–Mo–S unsupported catalysts by a one-step hydrothermal method for *p*-cresol hydrodeoxygenation. Ind Eng Chem Res 53:19001–19009

11. Wang CL, Wu ZZ, Tang CY, Li LH, Wang DZ (2013) The effect of nickel content on the hydrodeoxygenation of 4-methylphenol over unsupported NiMoW sulfide catalysts. Catal Commun 32:76–80

12. Yadav GD, Nair JJ (1999) Sulfated zirconia and its modified versions as promising catalysts for industrial processes. Microporous Mesoporous Mater 33:1–48

13. Romero Y, Richard F, Brunet S (2010) Hydrodeoxygenation of 2-ethylphenol as a model compound of bio-crude over sulfided Mo-based catalysts: promoting effect and reaction mechanism. Appl Catal B-Environ 98:213–223

14. Wang C, Wittreich CR, Lin C, Huang RJ, Vlachos DG, Gorte RJ (2020) Hydrodeoxygenation of *m*-cresol over Pt-WO_x/C using H_2 generated in situ by n-hexane dehydrogenation. Catal Lett 150:913–921

15. Wu K, Li XX, Wang WY, Huang YP, Jiang QK, Li WS, Chen YQ, Yang YQ, Li CZ (2022) Creating edge sites within the basal plane of a MoS_2 catalyst for substantially enhanced hydrodeoxygenation activity. ACS Catal 12:8–17

16. Xiang YZ, Li XN, Lu CS, Ma L, Yuan JF, Feng F (2011) Reaction performance of hydrogen from aqueous-phase reforming of methanol or ethanol in hydrogenation of phenol. Ind Eng Chem Res 50:3139–3144

17. Shafaghat H, Rezaei PS, Daud WMAW (2016) Using decalin and tetralin as hydrogen source for transfer hydrogenation of renewable lignin-derived phenolics over activated carbon supported Pd and Pt catalysts. J Taiwan Inst Chem Eng 65:91–100

18. Mao BW, Zhao AG, Huang MY, Jiang YY (2000) Preparation of a methylsulfo-methylcellulose-Pd complex and its catalytic behaviors in asymmetric hydrogenation of *o*-cresol. Polym Adv Technol 11:254–257

19. Shu RY, Li RX, Liu Y, Wang C, Liu PF, Chen Y (2020) Enhanced adsorption properties of bimetallic RuCo catalyst for the hydrodeoxygenation of phenolic compounds and raw lignin-oil. Chem Eng Sci 227:115920–115928

20. Munnik P, Jongh PED, Jong KPD (2014) Control and impact of the nanoscale distribution of supported cobalt particles used in Fischer–Tropsch catalysis. J Am Chem Soc 136:7333–7340

21. Lin DY, Duan P, Yang WT, Liu YF, Pan QH (2020) Facile controlled synthesis of core–shell/yolk–shell/hollow ZIF-67@Co-LDH/SiO_2 via a self-template method. Inorg Chem Front 7:1643–1650

22. Du YC, Wang F, Xia XY, Zhu H, Zhang Z, You CQ, Jiang XX, Jiang JC, Li CZ (2022) MOF-derived Co nanoparticle on nitrogen-rich carbon for fatty acid hydrotreatment into green diesel. Renewable Energy 198:246–253

23. Bo YN, Wang XR, Deng XT, Ma XB (2020) Imprint of free space around acid site in hollow mesoporous polymeric solid acid and application in heterogeneous acetal hydrolysis/asymmetric aldol tandem reaction. Appl Catal A-Gen 590:117360–117368

24. Hu Z, Han MM, Chen C, Zou ZD, Shen Y, Zhen F, Zhu XG, Zhang YX, Zhang HM, Zhao HJ, Wang GZ (2022) Hollow carbon sphere encapsulated nickel nanoreactor for aqueous-phase hydrogenation-rearrangement tandem reaction with enhanced catalytic performance. Appl Catal B-Environ 306:121140–121152

25. Wei ZZ, Li Y, Wang J, Li HR, Wang Y (2018) Chemoselective hydrogenation of phenol to cyclohexanol using heterogenized cobalt oxide catalysts. Chin Chem Lett 29:815–818

26. Li AQ, Shen K, Chen JY, Li Z, Li YW (2017) Highly selective hydrogenation of phenol to cyclohexanol over MOF-derived non-noble Co-Ni@NC catalysts. Chem Eng Sci 166:66–76

27. Shao YH, Xu J, Low ZX, Chen CH, Jiang H, Chen RZ (2022) A simple and versatile synthesis strategy of hollow MOFs for CO_2 separation and catalysis. Chem Commun 58:7944–7947

28. Qiao CX, Jia WL, Zhong QM, Liu BY, Zhang YF, Meng CG, Tian FP (2020) MOF-derived Cu-nanoparticle embedded in porous carbon for the efficient hydrogenation of nitroaromatic compounds. Catal Lett 150:3394–3401

29. Chen RY, Fang XY, Li ZG, Liu ZM (2022) Selective catalytic reduction of NO_x with NH_3 over a novel MOF-derived MnO_x catalyst. Appl Catal A-Gen 643:118754–118762

30. Wu W, Zhang W, Long Y, Qin JH, Ma JT (2021) MOF-derived Fe–N–C with interconnected mesoporous structure for halonitrobenzenes hydrogenation: role of dicyandiamide on the growth of active sites and pore structure. Microporous Mesoporous Mater 328:111472–111482

31. Li YB, Wee LH, Martens JA, Vankelecom IFJ (2017) Interfacial synthesis of ZIF-8 membranes with improved nanofiltration performance. J Membr Sci 523:561–566

32. Ma P, Ding ML, Liu X, Rong W, Yao JF (2022) Bimetallic zeolitic imidazolate framework derived magnetic catalyst for high-efficiency CO_2 chemical fixation. Chem Eng Sci 252:117530–117537

33. Jiang H, Wang SQ, Chen QQ, Du Y, Chen RZ (2022) ZIF-derived Co/Zn bimetallic catalytic membrane with abundant CNTs for highly efficient reduction of p-nitrophenol. Ind Eng Chem Res 61:7862–7873

34. Yu SZ, Luo SH, Zhan Y, Huang HB, Wang Q, Zhang YH, Liu YG, Hao AI (2020) Metal-organic framework-derived cobalt nanoparticle space confined in nitrogen-doped carbon polyhedra networks as high-performance bifunctional electrocatalyst for rechargeable Li–O_2 batteries. J Power Sources 453:227899–227906

35. Tang C, Zhang Q (2017) Nanocarbon for oxygen reduction electrocatalysis: dopants, edges, and defects. Adv Mater 29:1604103–1604111

36. Wang JC, Chaemchuen S, Chen C, Heynderickx PM, Roy S, Verpoort F (2022) N-functionalized hierarchical carbon composite derived from ZIF-67 and carbon foam for efficient overall water splitting. J Ind Eng Chem 105:222–230

37. Nagmani KA, Puravankara S (2022) Optimizing ultramicroporous hard carbon spheres in carbonate ester-based electrolytes for enhanced sodium storage in half-/full-cell sodium-ion batteries. Battery Energy 1:220007–220017

38. Zhao JB, Yang WC, Yuan HF, Li XM, Bing WZ, Han LF, Wu KL (2022) ZIF-8@ZIF-67 derived Co/NPHC catalysts for efficient and selective hydrogenation of nitroarenes. Catal Lett. https://doi.org/10.1007/s10562-022-04016-0

39. Li ZH, Liu RJ, Tang C, Wang ZY, Chen X, Jiang YH, Wang CZ, Yuan Y, Wang WB, Wang DB, Chen SN, Zhang XY, Zhang Q, Jiang JK (2020) Cobalt nanoparticles and atomic sites in nitrogen-doped carbon frameworks for highly sensitive sensing of hydrogen peroxide. Small 16:1902860–1902867

40. Dong XB, Zhao CY, Guan QX, Li W, Xu XF (2018) Metal-organic framework-derived cobalt and nitrogen co-doped porous carbon with four-coordinated Co–N_x for efficient acetylene hydrochlorination. Appl Organometal Chem 32:4570–4584

41. Du WF, Han FY, Zhang MW, Qian C, Yang XF (2021) Temperature-dependent synthesis of MOF-derived Co@N-doped carbon nanotube nanocomposites toward accelerated reduction of 4-nitrophenol. Compos Commun 25:100718–100723

42. Liu XH, Xu LJ, Xu GY, Jia WD, Ma YF, Zhang Y (2016) Selective hydrodeoxygenation of lignin-derived phenols to cyclohexanols or cyclohexanes over magnetic CoN_x@NC catalysts under mild conditions. ACS Catal 6:7611–7620

43. Yang YF, Jia LT, Hou B, Li DB, Wang JG, Sun YH (2014) The correlation of interfacial interaction and catalytic performance of N-doped mesoporous carbon supported cobalt nanoparticles for fischer-tropsch synthesis. J Phys Chem C 118:268–277

44. Chu CS, Rao S, Ma ZF, Han HL (2019) Copper and cobalt nanoparticles doped nitrogen-containing carbon frameworks derived from CuO-encapsulated ZIF-67 as high-efficiency catalyst for hydrogenation of 4-nitrophenol. Appl Catal B-Environ 256:117792–117800

45. Peng W, Yang XX, Mao LC, Jin JH, Yang SL, Zhang JJ, Li G (2021) ZIF-67-derived Co nanoparticles anchored in N doped hollow carbon nanofibers as bifunctional oxygen electrocatalysts. Chem Eng J 407:127157–127167

46. Zhu XR, Zhang JX, Jiang H, Chen RZ (2022) Pd nanoparticles decorated ZIFs/polymer core-shell nanofibers derived hierarchically porous N-doped carbon for efficient catalytic conversion of phenol. Appl Catal A-Gen 634:118538–118550

47. Zhang PF, Gong YT, Li HR, Chen ZR, Wang Y (2013) Solvent-free aerobic oxidation of hydrocarbons and alcohols with Pd@N-doped carbon from glucose. Nat Commun 4:1593–11603

48. Xie WC, Liu B, Liu YJ, Chen HB, Yang M, Li HM (2021) Co/N-codoped porous carbons derived from poly(schiff base)/Co(II) complex as ultrahighly efficient catalysts for CTH of nitroarenes. Appl Catal A-Gen 623:118249–118258

49. Shafaghat H, Rezaei PS, Daud WMAW (2015) Catalytic hydrogenation of phenol, cresol and guaiacol over physically mixed catalysts of Pd/C and zeolite solid acids. RSC Adv 5:33990–33998

50. Douka AI, Xu YY, Yang H, Zaman S, Yan Y, Liu HF, Salam MA, Xia BY (2020) A zeolitic-imidazole frameworks-derived interconnected macroporous carbon matrix for efficient oxygen electrocatalysis in rechargeable zinc-air batteries. Adv Mater 32:2002170–2002177

51. Tian LL, He GG, Cai YH, Wu SP, Su YY, Yan HQ, Yang C, Chen YL, Li L (2018) Co_3O_4 based nonenzymatic glucose sensor with high sensitivity and reliable stability derived from hollow hierarchical architecture. Nanotechnol 29:75502

52. Wu XS, Tan CL, He CM, Zhao T, Wu XW, Ma ZL, Wang HQ, Cai YZ, Wu Q, Li QY (2022) Strategy for boosting Co-N_x content for oxygen reduction reaction in aqueous metal-air batteries. J Power Sources 520:230891–230901

53. Shao YH, Zhang JX, Du Y, Jiang H, Liu YF, Chen RZ (2019) Controllable structure and basic sites of Pd@N-doped carbon derived from Co/Zn-ZIFs: role of Co. Ind Eng Chem Res 58:14678–14687

54. Wang WY, Wu K, Liu PL, Li L, Yang YQ, Wang Y (2016) Hydrodeoxygenation of p-cresol over Pt/Al_2O_3 catalyst promoted by ZrO_2, CeO_2, and CeO_2-ZrO_2. Ind Eng Chem Res 55:7598–7603

55. Wang DW, Wei J, Wang J, Wang SP, Zhou JC, Cai JJ (2022) MOFs carbonization: in-situ encapsulation of Co-species into N-doped carbons as highly efficient catalysts for nitrobenzene hydrogenation. Diamond Relat Mater 121:108748–108756

56. Zhang YY, Jia Y, Li M, Hou LA (2018) Influence of the 2-methylimidazole/zinc nitrate hexahydrate molar ratio on the synthesis of zeolitic imidazolate framework-8 crystals at room temperature. Sci Rep 8:9597–9603

57. Qasem MAA, Khan A, Onaizi SA, Mohaned HD, Helal A, Aziz A (2019) Effect of $Co(NO_3)_2 \cdot 6H_2O$ thermal decomposition temperature on the nano-Co_3O_4 product morphology and electrocatalysis of water oxidation. J Appl Electrochem 49:251–259

58. Li JL, Liu GL, Long XD, Gao G, Wu J, Li FW (2017) Different active sites in a bifunctional Co@N-doped graphene shells based catalyst for the oxidative dehydrogenation and hydrogenation reactions. J Catal 355:53–62

59. Yu ZQ, Wang AJ, Liu S, Yao YL, Sun ZC, Li X, Liu YY, Wang Y, Camaionic DM (2019) Hydrodeoxygenation of phenolic compounds to cycloalkanes over supported nickel phosphides. Catal Today 319:48–56

60. Tong L, Cai B, Zhang RH, Feng JF, Pan H (2022) In situ hydrodeoxygenation of lignin-derived phenols with synergistic effect between the bimetal and Nb_2O_5 support. Front Energy Res 9:746109–746121

61. Yu ZQ, Wang Y, Zhang GQ, Sun ZC, Liu YY, Shi C, Wang W, Wang AJ (2022) A highly dispersed Ni_3P/HZSM-5 catalyst for hydrodeoxygenation of phenolic compounds to cycloalkanes. J Catal 410:294–306

Authors and Affiliations

Chaoqun Fan[1] · Hang Zhu[1] · Jiuxuan Zhang[1] · Hong Jiang[1] · Rizhi Chen[1]

1   State Key Laboratory of Materials-Oriented Chemical
     Engineering, Nanjing Tech University, Nanjing 211816,
     China